Front. Optoelectron. 2015, 8(2): 128–140
DOI 10.1007/s12200-015-0475-1

REVIEW ARTICLE

Technology developments and biomedical applications of polarization-sensitive optical coherence tomography

Zhenyang DING, Chia-Pin LIANG, Yu CHEN (✉)

Fischell Department of Bioengineering, University of Maryland, College Park, MD 20742, USA

Abstract Polarization-sensitive optical coherence tomography (PS-OCT) enables depth-resolved mapping of sample polarization information, such as phase-retardation and optical axis orientation, which is particularly useful when the nano-scale organization of tissue that are difficult to be observed in the intensity images of a regular optical coherence tomography (OCT). In this review, we survey two types of methods and systems of PS-OCT. The first type is PS-OCT with single input polarization state, which contain bulk optics or polarization maintaining fiber (PMF) based systems and single-mode fiber (SMF) based systems. The second type is PS-OCT with two different input polarization states, which contain SMF based systems and PMF based systems, through either time, frequency, or depth multiplexing. In addition, representative biomedical applications using PS-OCT, such as retinal imaging, skin cancer detection, and brain mapping, are demonstrated.

Keywords optical coherence tomography (OCT), polarization-sensitive optical coherence tomography (PS-OCT), polarization, imaging

1 Introduction

Polarization-sensitive optical coherence tomography (PS-OCT) [1] is a functional extension of optical coherence tomography (OCT) [2]. By measuring the polarization state of light reflecting or scattering back from tissue, PS-OCT enables depth-resolved mapping of sample polarization information, such as phase-retardation and optical axis orientation. Polarization information is particularly useful when the nano-scale organization of tissue is difficult to be observed in the intensity images of a regular OCT. The potential of PS-OCT for biomedical applications has been demonstrated in numerous areas, including dermatology (such as imaging burn lesion of skin [3–9] and skin tumor [10,11]), ophthalmology (such as cornea [12,13], retina [14–22], and anterior eye chamber [23] imaging), dentistry [24–28], endoscopy [29], cardiology [30,31], pulmonlogy [32], osteology [33,34], and neurology [35–37].

In general, there are two main types of PS-OCT methods. The first type is PS-OCT systems with single input polarization state. The second type is PS-OCT system with two input polarization states. In these two types, they both contain two subtypes of configurations: polarization maintaining (PM) and non-PM systems, respectively. Table 1 summarizes the key features of these different types of PS-OCT systems.

In PS-OCT systems with single input polarization state, one subtype is PM configuration containing bulk optics or polarization maintaining fiber (PMF) based systems. The OCT signal is measured with polarization sensitive detectors [1,38–42]. PM configuration has the advantage that the input polarization state can be well-defined and can achieve stable polarization imaging with simple algorithm and system scheme. However, this configuration using PMF can cause imaging artifacts, i.e., the "ghost peaks" due to crosstalk between the orthogonal polarization channels of PMF. This problem can be solved by adding long (20 – 30 m) PMF in the arms of the interferometer to shift those peaks to a position, where it doesnot impact the sample image [40,42].

The other subtype is non-PM configuration, namely, single-mode fiber (SMF) based system. Using SMF and SMF based components reduces system complexity, artifacts, and cost [43,44]. In this subtype, several polarization controllers are applied in the SMF based system to adjust the polarization state of the system. There are two approaches for SMF based PS-OCT with single input polarization state. The first one calibrates the input light onto the sample to a circularly polarized light using polarization controller [43]. The algorithm for calculating phase retardance and optical axis orientation is the same as

Received July 30, 2014; accepted November 19, 2014

E-mail: yuchen@umd.edu

Table 1 Summary of different PS-OCT configurations

type	sub-type	pros	cons	reference
single input polarization state	PMF and bulk optics	• simple algorithm • no need for calibration • stable	• ghost peak • high cost • no local birefringence • no diattenuation	[1,38–42]
	SMF	• simple system and algorithm • low cost • no ghost peak	• need calibration • not very stable • no local birefringence • no diattenuation	[43,44]
two input polarization states	SMF	• local birefringence • diattenuation	• complex system (modulation or multiplex) • high cost • complex algorithm	[19,23,45,46]
	PMF and bulk optics	• local birefringence • diattenuation	• complex system (modulation or multiplex) • high cost • complex algorithm	[30,47–50]

Notes: PMF, polarization maintaining fiber; SMF, single-mode fiber

those used in PM system. Alternatively, we recently develop another method to calibrate the phase retardance of the SMF system to multiple integers of π using a quarter wave plate (QWP) [44].

Although PS-OCT system with single input polarization state has the advantage of simpler algorithm and scheme, the polarization information obtained is cumulated from the sample surface to the measurement depth. Therefore, the "local" polarization information cannot be obtained accurately.

The second type, PS-OCT system with two different input polarization states, can improve the quantification accuracy of local polarization information. In this category, one subtype is non-PM configuration, namely, SMF based systems [23,45], and the other subtype is PM configuration [30,47–50]. Compared with the PS-OCT with single input polarization state, using two independent input polarization states can obtain local polarization information using matrix similarity and eigenvalues. One way to obtain the information from two polarization states input is to time-multiplex the input signal, i.e., alternating the input light polarization state for each A-line [23,45]. Since the two adjacent A-lines are closely placed, they will provide the polarization information from the overlapped sampling area. However, in endoscopic or catheter-based imaging, sample motion or stress-induced birefringence changes in the fiber-optic probe can be non-negligible during the time interval between successive A-lines [29], resulting a less accurate estimation of local polarization information.

To overcome this limitation, techniques for multiplexing the two polarization states during one axial scan acquisition have been developed [19,22,46,51,52]. There are two main approaches. One uses frequency multiplexing to encode two input polarization state information with different frequencies [22,46,51,52]. However, the electro-optic or acousto-optic devices used for frequency shifting not only add to system cost, but also significantly increase system complexity as they require dedicated high speed control. The other approach employs a passive polarization delay unit for depth multiplexing [19]. In this approach, the passive polarization delay unit induces different sample arm path lengths for orthogonally polarized light, thereby enabling simultaneous detection of the polarization sensitive information for two incident states. However, this approach needs a light source with long coherence length to avoid depth degeneracy [53].

In this review, we summarize the principles and key technologies of these methods. We will discuss the advantages and challenges of each method. In addition, representative biomedical applications using PS-OCT, such as retinal imaging, skin cancer detection, and brain mapping, are demonstrated.

2 Principle of PS-OCT

2.1 PS-OCT with single input polarization state

PS-OCT systems with single input polarization state contain two subtypes: PM and non-PM configurations. The first subtype uses PM components such as bulk optics or PMF. This method has been widely adopted for PS-OCT [1,38–42]. The time-domain version of this method was first presented by Hee et al. in 1992 [1]. More recently, frequency-domain (including both sweep-source and spectral-domain) PS-OCT has been developed as well [38,40–42].

Basically, this method uses a circularly-polarized light to illuminate the sample, yielding phase retardance measurement insensitive to sample orientation in the lateral directions. Phase retardance and relative axis orientation of the sample can be measured by this method directly. As the polarization information of polarization maintaining system is known, it only needs a single polarization state to obtain axis orientation and phase retardance information. Figure 1 shows the schematics of a sweep-source PS-OCT

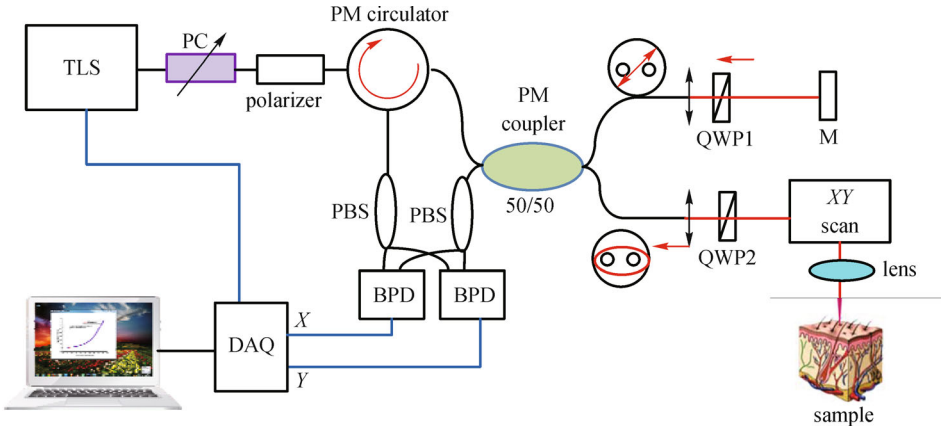

Fig. 1 Scheme of sweep-source PS-OCT with PM fiber using single input polarization state [42]. TLS, tunable laser source; PC, polarization controller; QWP, quarter wave plate; M, mirror; *XY* scan, galvo scanner; PBS, polarizing beam splitter; BPD, balanced photodetector; DAQ, data acquisition card. Reproduced from Ref. [42] with permission

with PM fiber. Similarly, this configuration can be extended to time- or spectral-domain PS-OCT as well.

The basic principle of this method has been presented previously [1,39,41]. The reference light exiting the PM fiber of the 50:50 coupler is linearly polarized along the slow axis of the fiber. QWPs are needed to set in the system to adjust the polarization state of the light in the reference and sample arm of the system. The Jones matrix of QWP can be expressed as [39]

$$\boldsymbol{J}_{\mathrm{QWP}} = \boldsymbol{R}(\theta)\begin{bmatrix} \mathrm{e}^{\mathrm{j}\pi/4} & 0 \\ 0 & \mathrm{e}^{-\mathrm{j}\pi/4} \end{bmatrix}\boldsymbol{R}(-\theta), \tag{1}$$

where the rotation matrix $\boldsymbol{R}(\theta) = \begin{bmatrix} \cos\theta & \sin\theta \\ -\sin\theta & \cos\theta \end{bmatrix}$.

As there is no circular birefringence in QWP, The forward and backward propagation matrix of QWP is equal as $\overleftarrow{\boldsymbol{J}}_{\mathrm{QWP}} = \overrightarrow{\boldsymbol{J}}_{\mathrm{QWP}}$ [54]. In the reference arm, it traverses a QWP oriented at 22.5° to the slow axis. After reflection at the reference mirror and double-passing the QWP, the light is in a linear polarization state oriented at 45° to the slow axis, providing equal reference optical field $\boldsymbol{E}_{\mathrm{R}}$ in both the fast and slow axes of the fiber.

$$\begin{aligned} \boldsymbol{E}_{\mathrm{R}} &= \frac{1}{\sqrt{2}}\overleftarrow{\boldsymbol{J}}_{\mathrm{QWP1}}\overrightarrow{\boldsymbol{J}}_{\mathrm{QWP1}}\begin{bmatrix} 0 \\ 1 \end{bmatrix} \\ &= \frac{1}{\sqrt{2}}\boldsymbol{J}_{\mathrm{QWP1}}\boldsymbol{J}_{\mathrm{QWP1}}\begin{bmatrix} 0 \\ 1 \end{bmatrix} = \frac{1}{2}\begin{bmatrix} 1 \\ -1 \end{bmatrix}. \end{aligned} \tag{2}$$

Here, $\boldsymbol{J}_{\mathrm{QWP1}}$ is the Jones matrix of QWP at 45° to the slow axis. The sample light exiting the sample arm fiber is also polarized along the slow axis of the fiber. It traverses a QWP oriented at 45° to the slow axis with Jones matrix $\boldsymbol{J}_{\mathrm{QWP2}}$, resulting circularly polarized light on the sample. The Jones matrix of the sample $\boldsymbol{J}_{\mathrm{S}}$ with phase retardance δ and fast axis orientation θ can be expressed as [54]

$$\boldsymbol{J}_{\mathrm{S}} = \begin{pmatrix} \mathrm{e}^{\mathrm{j}\frac{\delta}{2}}\cos^2\theta + \mathrm{e}^{-\mathrm{j}\frac{\delta}{2}}\sin^2\theta & (\mathrm{e}^{\mathrm{j}\frac{\delta}{2}} - \mathrm{e}^{-\mathrm{j}\frac{\delta}{2}})\sin\theta\cos\theta \\ (\mathrm{e}^{\mathrm{j}\frac{\delta}{2}} - \mathrm{e}^{-\mathrm{j}\frac{\delta}{2}})\sin\theta\cos\theta & \mathrm{e}^{\mathrm{j}\frac{\delta}{2}}\sin^2\theta + \mathrm{e}^{-\mathrm{j}\frac{\delta}{2}}\cos^2\theta \end{pmatrix}. \tag{3}$$

As the circular birefringence in sample is neglected, the forward and backward propagation matrix of sample is equal as $\overleftarrow{\boldsymbol{J}}_{\mathrm{S}} = \overrightarrow{\boldsymbol{J}}_{\mathrm{S}}$ [54]. The Jones vector of the sample beam, after exiting the interferometer, $\boldsymbol{E}_{\mathrm{SZ}}$, is

$$\begin{aligned} \boldsymbol{E}_{\mathrm{SZ}} &= \frac{1}{\sqrt{2}}\boldsymbol{J}_{\mathrm{QWP2}}\boldsymbol{J}_{\mathrm{S}}\sqrt{R(z)}\boldsymbol{J}_{\mathrm{S}}\boldsymbol{J}_{\mathrm{QWP2}}\begin{bmatrix} 0 \\ 1 \end{bmatrix} \\ &= \frac{\sqrt{R(z)}}{\sqrt{2}}\begin{bmatrix} \cos\delta\exp(-\mathrm{j}\delta) \\ \sin\delta\exp[\mathrm{j}(\pi-\delta-2\theta)] \end{bmatrix}. \end{aligned} \tag{4}$$

The AC coupled interference signals $\boldsymbol{I}$ at depth z of the sample can be expressed as

$$\begin{aligned} \boldsymbol{I} &= \begin{bmatrix} I_X \\ I_Y \end{bmatrix} = \begin{bmatrix} E_{rx}E_{sx}^* + E_{rx}^*E_{sx} \\ E_{ry}E_{sy}^* + E_{ry}^*E_{sy} \end{bmatrix} \\ &= \frac{\sqrt{R(z)}}{\sqrt{2}}\begin{bmatrix} \cos\delta\cos(kz-\delta) \\ \sin\delta\cos(kz+\pi-\delta-2\theta) \end{bmatrix}. \end{aligned} \tag{5}$$

The interference signals at orthogonal polarization axes X and Y is split by the polarizing fiber beam splitter PBS and detected by two balanced photodetectors respectively. Fast Fourier transform (FFT) can be used to process these two interference signals. A_X and A_Y are the amplitude of the interference signals at X and Y axes, respectively. ϕ_X and ϕ_Y are the phase of the interference signals at X and Y axes. The phase retardance of the sample can be written as [39]

$$\delta = \arctan\frac{A_Y}{A_X}. \tag{6}$$

The fast axis orientation can be written as [39]

$$\theta = (\pi - \phi_X + \phi_Y)/2. \tag{7}$$

In this method, δ calculated from Eq. (6) represents the retardance value cumulated from the sample surface to the measurement depth. To measure the specific polarization feature at a specific depth, depth-resolved "local" retardance needs to be determined. Such local retardance was previously estimated using the retardance difference between adjacent depths (the "differential retardance") [7]. However, Fan and Yao [30,47,48] show that such calculation is valid only in samples with constant optical axis over depth. In samples whose optical axis varies with depth, the measured cumulative retardance is not equal to the summation of the local retardance from all top layers. In addition, the diattenuation of sample is not considered in this method. When the sample has strong diattenuation, this method will be ineffective.

The second subtype of this category is non-PM system, namely, using SMF components and SMF with single input polarization state [43,44]. In this subtype, several polarization controllers are applied in the SMF based system to adjust the polarization information of the system. There are two approaches in this subtype. The first one calibrates the light sending onto the sample to circular polarization using polarization controllers. The algorithm for calculating phase-retardation and optical axis orientation is the same as those used in PM system (Eqs. (1)–(7)) [43]. However, this method needs a complex polarization controlling process. In the second method, a QWP is acted as a calibration standard on the sample arm, and a polarization controller is used to adjust the output stokes vector of the front and back surfaces of the QWP to [0, 0, 1]$^{\mathrm{T}}$ and [0, 0, −1]$^{\mathrm{T}}$, respectively. In this way, the phase retardance of the SMF system is calibrated to multiple integers of π, and the phase retardance and optics axis orientation can be measured reliably [44].

2.2 PS-OCT system with two different input polarization states

The second type, PS-OCT system with two different input polarization states, also contains both PM and non-PM configurations. Using two independent polarization states, one can extract the complete set of local polarization properties including local retardance, local diattenuation, and local axis orientation using Jones matrix based PS-OCT. The key of this method is using matrix similarity and eigenvalues. The principle of this method has been presented previously [23,30,47,48].

Here, we first describe the non-PM system, namely, SMF based system. In Fig. 2, the schematic diagram of a SMF-based PS-OCT is shown. To measure the Jones matrix of a sample, the states of polarization of the backscattered light with at least two incident states should be measured.

Input incident polarization state $\boldsymbol{E}_{\mathrm{in}}$ can be expressed as [23]

$$\boldsymbol{E}_{\mathrm{in}} = \begin{bmatrix} H_{\mathrm{in1}} & H_{\mathrm{in2}} \\ V_{\mathrm{in1}} & V_{\mathrm{in2}} \end{bmatrix} = \begin{bmatrix} 1 & 0 \\ 0 & \mathrm{e}^{\mathrm{i}\varphi} \end{bmatrix}, \tag{8}$$

where H_{in1}, H_{in2}, V_{in1} and V_{in2} are the electric field of two input incident lights on the horizontal and vertical channels. φ is the phase difference between two input incident lights.

The reference light needs to balance the orthogonal

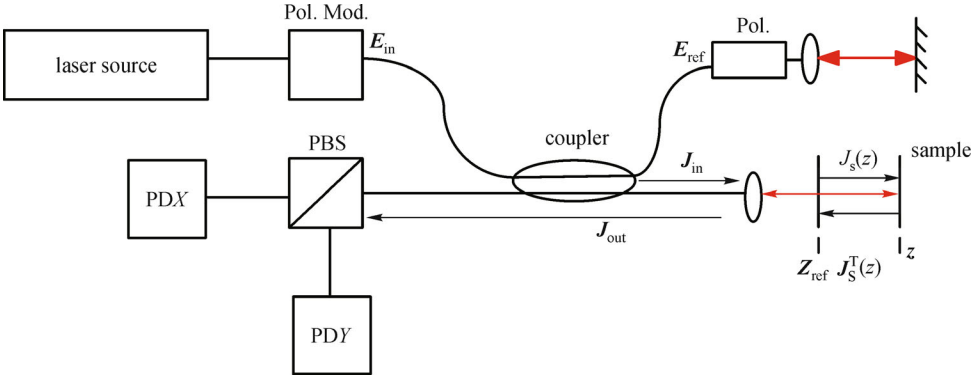

Fig. 2 Schematic diagram of a fiber-based PS-OCT with two different input polarization state [23]. Pol. Mod., polarization modulator; Pol., polarization controller. In the case of time-domain and spectral-domain OCTs, the light source is a broadband light source. It is a wavelength-swept light source for swept-source OCT. PDX and PDY are photodetection devices to detect the orthogonal polarization axes X and Y. Photodetection devices are photodetectors for time-domain and swept-source OCTs, and they are spectrometers for spectral-domain OCT. Typically the polarizer is introduced in the reference arm to deliver the same optical power of reference beam to two photodetectors. Reproduced from Ref. [23] with permission

polarization axes X and Y, which can be expressed as [23]

$$\boldsymbol{E}_{\text{ref}} = \begin{bmatrix} H_{\text{ref}} & 0 \\ 0 & V_{\text{ref}} \end{bmatrix} = \begin{bmatrix} 1 & 0 \\ 0 & \mathrm{e}^{\mathrm{i}\psi} \end{bmatrix}, \tag{9}$$

where H_{ref} and V_{ref} are the electric field of the reference light on the horizontal and vertical channels. ψ is phase difference between the reference light on the horizontal and vertical channels. The amplitude of the reference light on the horizontal and vertical channels are equal by adjusting the polarization controller on the reference arm.

Assuming $\boldsymbol{J}_{\text{ST}}$ is the round-trip Jones matrix of the sample and $\boldsymbol{J}_{\text{ST}} = \boldsymbol{J}_{\text{S}}^{\text{T}}(z_i)\boldsymbol{J}_{\text{S}}(z_i)$ [23], and $\boldsymbol{J}_{\text{in}}$, $\boldsymbol{J}_{\text{out}}$ represent the Jones matrix of the optical fibers of the input and output paths. The measured Jones matrix signals $\boldsymbol{S}(z_i)$ at the sample depth z_i can be written as

$$\begin{aligned} \boldsymbol{S}(z_i) &= \boldsymbol{E}_{\text{ref}}\boldsymbol{J}_{\text{out}}\boldsymbol{J}_{\text{ST}}\boldsymbol{J}_{\text{in}}\boldsymbol{E}_{\text{in}} \\ &= \begin{bmatrix} 1 & 0 \\ 0 & \mathrm{e}^{\mathrm{i}\psi} \end{bmatrix}\boldsymbol{J}_{\text{out}}\boldsymbol{J}_{\text{ST}}(z_i)\boldsymbol{J}_{\text{in}}\begin{bmatrix} 1 & 0 \\ 0 & \mathrm{e}^{\mathrm{i}\varphi} \end{bmatrix} \\ &= \begin{bmatrix} 1 & 0 \\ 0 & \mathrm{e}^{\mathrm{i}\psi} \end{bmatrix}\boldsymbol{J}_{\text{out}}\boldsymbol{J}_{\text{S}}^{\text{T}}(z_i)\boldsymbol{J}_{\text{S}}(z_i)\boldsymbol{J}_{\text{in}}\begin{bmatrix} 1 & 0 \\ 0 & \mathrm{e}^{\mathrm{i}\varphi} \end{bmatrix}. \end{aligned} \tag{10}$$

$\boldsymbol{S}(z_{i+1})$ at the sample depth z_{i+1} can be written as

$$\begin{aligned} \boldsymbol{S}(z_{i+1}) = &\begin{bmatrix} 1 & 0 \\ 0 & \mathrm{e}^{\mathrm{i}\psi} \end{bmatrix}\boldsymbol{J}_{\text{out}}\boldsymbol{J}_{\text{S}}^{\text{T}}(z_i)\boldsymbol{J}_{\text{ST}}(z_i,z_{i+1}) \\ &\cdot\boldsymbol{J}_{\text{S}}(z_i)\boldsymbol{J}_{\text{in}}\begin{bmatrix} 1 & 0 \\ 0 & \mathrm{e}^{\mathrm{i}\varphi} \end{bmatrix}, \end{aligned} \tag{11}$$

where $\boldsymbol{J}_{\text{ST}}(z_i,z_{i+1})$ is the round-trip Jones matrix of the sample z_i to z_{i+1}. The local measured Jones matrix signals $\boldsymbol{M}(z_{i+1},z_i)$ can be expressed as

$$\begin{aligned} \boldsymbol{M}(z_{i+1},z_i) =& \boldsymbol{S}(z_{i+1})\boldsymbol{S}(z_i)^{-1} \\ =& \begin{bmatrix} 1 & 0 \\ 0 & \mathrm{e}^{\mathrm{i}\psi} \end{bmatrix}\boldsymbol{J}_{\text{out}}\boldsymbol{J}_{\text{S}}^{\text{T}}(z_i)\boldsymbol{J}_{\text{ST}}(z_{i+1}) \\ &\cdot\boldsymbol{J}_{\text{S}}^{\text{T}}(z_i)^{-1}\boldsymbol{J}_{\text{out}}^{-1}\begin{bmatrix} 1 & 0 \\ 0 & \mathrm{e}^{\mathrm{i}\psi} \end{bmatrix}^{-1}, \end{aligned} \tag{12}$$

where

$$\begin{aligned} \boldsymbol{S}(z_i)^{-1} = &\begin{bmatrix} 1 & 0 \\ 0 & \mathrm{e}^{\mathrm{i}\varphi} \end{bmatrix}^{-1}\boldsymbol{J}_{\text{in}}^{-1}\boldsymbol{J}_{\text{S}}(z_i)^{-1} \\ &\cdot\boldsymbol{J}_{\text{S}}^{\text{T}}(z_i)^{-1}\boldsymbol{J}_{\text{out}}^{-1}\begin{bmatrix} 1 & 0 \\ 0 & \mathrm{e}^{\mathrm{i}\psi} \end{bmatrix}^{-1}. \end{aligned} \tag{13}$$

Equation (13) can be rewritten using a similarity transformation with the eigenvalues $\lambda_{1,2}$ as [23]

$$\boldsymbol{M}(z_{i+1},z_i) = \boldsymbol{A}\begin{bmatrix} \lambda_1 & 0 \\ 0 & \lambda_2 \end{bmatrix}\boldsymbol{A}^{-1}. \tag{14}$$

Here $\lambda_{1,2}$ and $\boldsymbol{A}$ are the eigenvalues and eigenvector matrix of $\boldsymbol{M}(z_{i+1},z_i)$, and

$$\boldsymbol{A} = \begin{bmatrix} 1 & 0 \\ 0 & \mathrm{e}^{\mathrm{i}\psi} \end{bmatrix}\boldsymbol{J}_{\text{out}}\boldsymbol{J}_{\text{S}}^{\text{T}}(z_i)\boldsymbol{R}(\theta), \tag{15}$$

where $\boldsymbol{J}_{\text{ST}}(z_{i+1})$ and $\boldsymbol{M}(z_{i+1},z_i)$ are similar matrix. The local phase retardation δ and relative-attenuation σ can be calculated from the eigenvalues $\lambda_{1,2}$ as [23]

$$\delta(z_{i+1},z) = \left|\tan^{-1}\frac{\text{Im}\left[\lambda_1/\lambda_2\right]}{\text{Re}\left[\lambda_1/\lambda_2\right]}\right|, \tag{16}$$

$$\sigma(z_{i+1},z) = \ln\left|\frac{\lambda_1}{\lambda_2}\right|. \tag{17}$$

In this method, the optic axis orientation cannot be obtained from $\boldsymbol{A}$ if the diattenuation in sample and fiber exists [23]. Fan and Yao [30,47,48] present a method to remove the diattenuation of $\boldsymbol{M}(z_{i+1},z_i)$ and then use eigen-decomposition to $\tilde{\boldsymbol{M}}(z_{i+1},z_i)$ in order to obtain optical axis orientation.

In addition, using SMF-based system with two different input polarization states, Park et al. present a method to calculate phase retardance and optical axis orientation using the space geometry relation of Stokes vector in Poincaré sphere [55].

In summary, the system scheme and demodulation algorithm of PS-OCT with two input polarization states are much more complex than those used in PS-OCT with single input polarization state as described in Section 2.1. However, using two input polarization states has two advantages: 1) It is possible to exact the local polarization properties and diattenuation; and 2) It can be implemented with SMF, which can be readily integrated with endoscopes or needle probes for clinical imaging.

In reality, during endoscopic or catheter-based imaging, sample motion or stress-induced birefringence changes in the fiber-optic probe can be non-negligible during the time interval between successive A lines. To overcome this limitation, two alternative SMF-based PS-OCT systems that can multiplex two polarization states in one axial scan acquisition have been developed. One approach modulates the two polarization states with different frequencies, namely, frequency multiplexing using electro-optic or acousto-optic devices. The other approach employs a passive polarization delay unit, namely, depth multiplexing.

Frequency-multiplex approach simultaneously illuminates and detects two polarization states, as depicted in Fig. 3. In this method, the light in the sample arm is split into two intrinsic polarization states. Each state is then

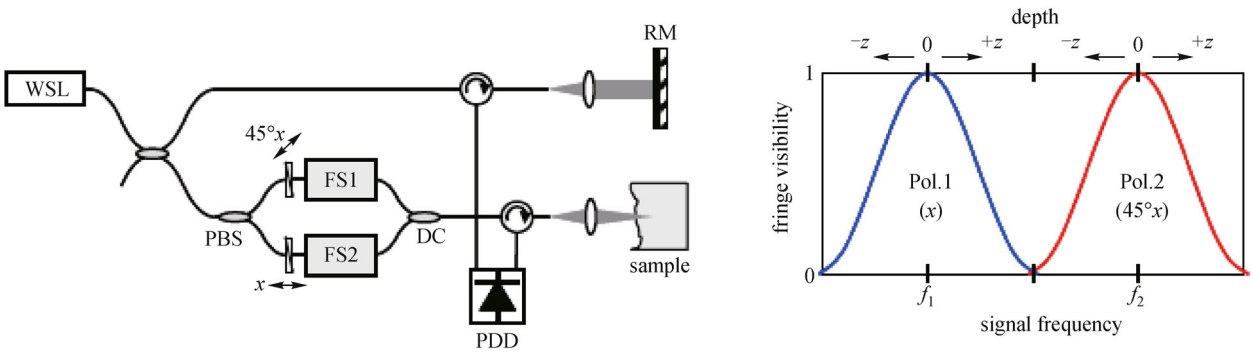

Fig. 3 Schematic diagram of a PS-OCT using frequency multiplexing [46]. WSL, wavelength-swept laser, RM, reference mirror; PDD, polarization diverse detection; PBS, polarization beam splitter; FS, frequency shifter; DC, directional coupler. Two polarization states occupy different electrical frequency bands, so the two polarization channels can be acquired simultaneously and demultiplexed in data processing. Reproduced from Ref. [46] with permission

encoded with a distinct frequency shift using electro-optic or acousto-optic devices prior to recombining the paths at a directional coupler. Since the two polarization states occupy different electrical frequency bands, the two polarization channels can be acquired simultaneously and demultiplexed in data processing, with additional benefit of avoiding depth degeneracy [53], i.e., it does not need a light source with long coherent length. However, in this type of method, the challenge is that the electro-optic or acousto-optic devices not only add to system cost, but also significantly increase system complexity since they require dedicated high speed control.

Depth-multiplex approach employs a passive polarization delay unit (PDU) to separate the information from the two polarization states [19]. In this method, a passive polarization dependent delay unit was added in the sample arm, as shown in Fig. 4. The PDU induces different sample arm path lengths for orthogonally polarized light, thus enabling the detection of the polarization sensitive information for two incident states simultaneously. The OCT signals originating from the two incident states are separated by Δz in depth. However, this method requires that the tunable light source has a long coherence length to avoid depth degeneracy.

PS-OCT with two input polarization states can also be implemented with PM components. Fan and Yao present a spectral-domain PM PS-OCT using bulk optics with two input polarization states [30,47–50]. This system [49,50] combines a dual-delay assembly in the reference arm to achieve independent vertically and horizontally polarized light detection. In this method, instead of separating the two orthogonal polarization channels in the detection arm,

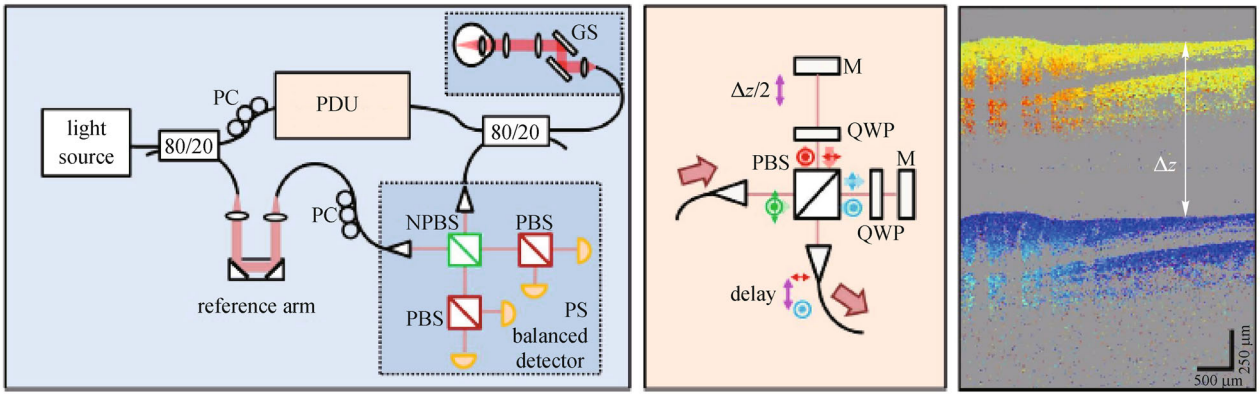

Fig. 4 Swept-source / Fourier domain OCT with a passive polarization delay unit [19]. (a) Scheme of PS-OCT with a polarization delay. The sample and reference beam interfere at the non-polarizing beam splitter and are then split up into orthogonal polarization X and Y by a polarizion beam splitters. The two orthogonal polarization channels are detected by two balanced photodetectors. (b) Scheme of the passive delay unit. (c) Representative image of the location difference between the orthogonal detection channels. The OCT signals originating from the two incident states are separated by Δz in depth. PC, polarization controller; PDU: polarization delay unit; GS, galvanometer scanner; PBS, polarizing beam splitter; NPBS, non-polarizing beam splitter; QWP, quarter wave plate; M, mirror. Reproduced from Ref. [19] with permission

two reference beams with different path lengths are used to separate the two orthogonal detection channels in the depth direction, which also can be considered as a form of depth multiplexing. The algorithm for calculating phaseretardance and optical axis orientation [30,47,48] is similar to the method of SMF based system with two input polarization states (Eq. (8) – (17)).

3 Biomedical applications of PS-OCT

There are numerous biomedical applications for PS-OCT including dermatology [3–11], ophthalmology [12–23], dentistry [24–28], endoscopy [29], cardiology [30,31], pulmonlogy [32], osteology [33,34], and neurology [35–37]. For example, in dentistry, PS-OCT provided better functional contrast and more detailed structural information than conventional OCT, which has the potential to be a powerful tool for research of dental formation and caries diagnosis [24–28]. In pulmonlogy, PS-OCT provides complementary information that may be leveraged to ensure that the collected specimens have high tumor content by avoiding tumor-negative tissues including fibrosis [32]. In osteology, PS-OCT could be a useful tool to study collagen organization within the intervertebral disc in vitro and possibly *in vivo* and its variation with applied load and disease [34]. Here, we focus on three important applications of PS-OCT: eye, skin, and brain.

3.1 PS-OCT imaging of eye

PS-OCT provides interesting new tissue specific information in ophthalmology. In cornea [12], the knowledge of the phase retardation and the optics axis distribution of the cornea might improve nerve fiber polarimetry for glaucoma diagnostics and could be useful for diagnosing different types of pathologies of the cornea [12]. In retina [14–22], PS-OCT enables the differentiation of several layers within the retina due to the different light-tissue interaction mechanisms. The retinal layers can be categorized into polarization preserving layers (e.g., photoreceptor layer), birefringent layers (e.g., retinal nerve fiber layer (RNFL), or Henle's fiber layer) [14–19,22], and depolarizing (polarization scrambling) layers (e.g., retinal pigment epithelium (RPE)) [20,21]. In anterior eye chamber [23], PS-OCT can quantitatively evaluate the risk of angle-closure glaucoma and detect the landmark structures, such as trabecular meshwork.

Here, we focus on the application of PS-OCT in RNFL [19]. RNFL birefringence can be assessed using PS-OCT system, which might be an important marker for glaucoma diagnostics in addition to the nerve fiber layer thickness. In this application, PS-OCT system is SMF-based with depth multiplex. Figures 5(a) and 5(b) are OCT fundus projection image and the color fundus photo. Figure 5(c) is the reflectivity image extracted from the same data volume. RNFL birefringence can be observed as a color change from blue to yellow in the corresponding phase retardation image in Fig. 5(d). A fundus phase retardation map is shown in Fig. 5(e). In this map, the birefringent RNFL is clearly visible around the optic disk. Some interaction between the birefringent Henle's fiber layer and uncompensated birefringence of the cornea can be observed in the fovea region. A similar retardation pattern around the optic disk can be observed in the RNFL map generated with a commercial scanning laser polarimeter in Fig. 5(f) [19].

This example demonstrates the ability of PS-OCT to measure the birefringence of RNFL. This is especially interesting for diagnosis of glaucoma. In addition, PS-OCT can reliably segment and identify the retinal pigment epithelium layer, which makes PS-OCT a valuable tool for age-related macular degeneration (AMD) diagnosis [21]. Therefore, PS-OCT might become a valuable tool for several clinical applications in ophthalmology.

3.2 PS-OCT imaging of skin

PS-OCT reveals birefringent regions within the dermis corresponding to the location of collagen fibers. Especially, the properties of collagen-rich tissues including tendon and scar tissues can be quantified [8]. For example, PS-OCT can detect thermal damage due to denaturation of collagen in porcine tendons. Similar changes in the polarization were observed in thermally injured porcine skin, which could be attributed to a reduction of birefringence, or a change in the scattering properties. Therefore, PS-OCT has the potential to image the structure of burned human skin over large areas, which would be of significant benefit to optimize the management of burn patients [3–7,9].

PS-OCT can also detect skin tumor or cancer [10,11]. Duan et al. use a polarization maintaining bulk optics PS-OCT system to image *ex vivo* samples of normal and cancerous mouse skin, which provides both intensity and birefringence images simultaneously. They use polarization contrast of mouse skin to discriminate basal cell carcinoma (BCC) from healthy tissues [11]. Figure 6 shows representative comparison images of the histology and OCT data sets. The top row shows images obtained from healthy mouse skin, and images in the middle and bottom rows were acquired from two types of BCCs samples, allograft and endogenous, respectively, each with different tumor sizes. In intensity OCT images, there often appeared a visible interface between either dermis and hypodermis or dermis and tumor. In phase retardation images, a trend of increasing retardation with penetration depth in dermis can be observed clearly, indicating the existence of birefringence; in contrast, tumorous regions were marked by a constant phase retardation, consistent with the expectation that the development of tumor would reduce birefringence in tissue by distorting the alignment of the collagen, so the polarization information can identify the tumor more accurately [11]. PS-OCT provides a multi-

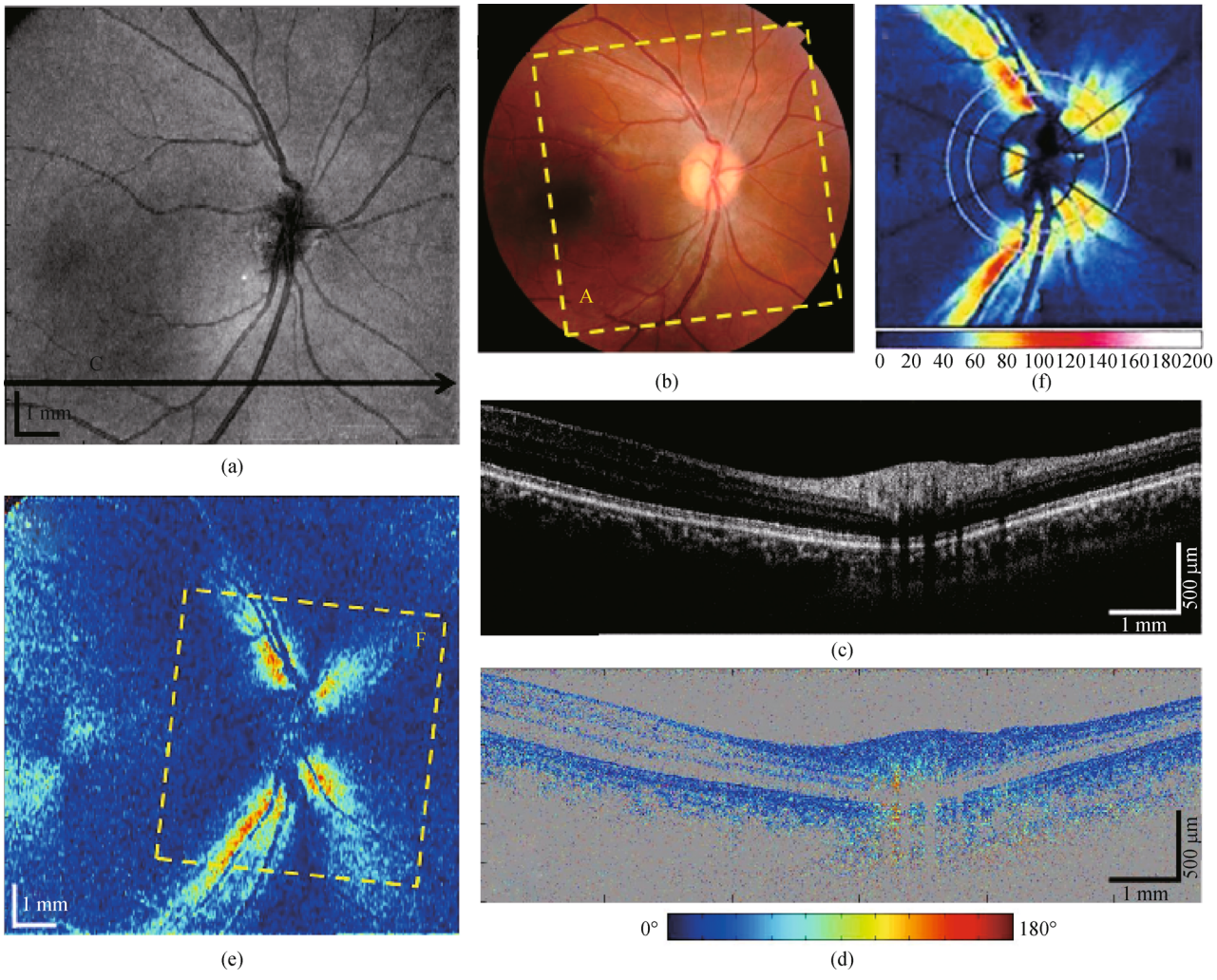

Fig. 5 Wide field PS-OCT imaging of the human retina [19]. (a) Fundus projection image. As indicated in the color fundus photo (b). (c) Reflectivity B-scan image on the location indicated by the arrow in (a). (d) Corresponding phase retardation image (color scale: 0°– 180°). Increasing phase retardation due to RNFL birefringence can be observed by a color change from blue to yellow. (e) Wide field fundus image of phase retardation (color scale: 0° – 27°). Strong birefringence can be observed around the optic disk along the nerve fiber bundles. (f) Scanning laser polarimetry image of the same eye taken with the Zeiss GDx. Color map below. The scanned area of 15° × 15° is indicated by the dashed rectangle in (e). Reproduced from Ref. [19] with permission

contrast information-based analysis that can achieve good accuracy for skin tumor detection. This study demonstrates the potential of PS-OCT for clinical skin cancer diagnosis.

3.3 PS-OCT imaging of brain

Imaging brain with PS-OCT opens up new applications in investigating neurological and psychiatric disorders [35–37]. For example, PS-OCT images are highly correlated with nerve fiber bundle location [37]. The nerve fiber bundles in the external and internal capsules could be identified clearly. Compared with conventional OCT, PS-OCT has the ability to visualize nerve fiber bundles at higher contrast. Therefore, PS-OCT has the potential to be an intraoperative imaging modality for neurosurgery [37]. More importantly, PS-OCT can provide anatomical information, differentiate between gray and white matters, and quantify fiber architectures and orientations in the brain, therefore it may offer a new solution for reconstruction of macroscopic tissues such as primate and human brains at microscopic resolution [35,36].

Wang et al. present an optical imaging and tractography of rat brain *ex vivo* using multi-contrast optical coherence tomography (MC-OCT) with polarization maintaining PS-OCT system, which is capable of simultaneously generating depth-resolved images of reflectivity, phase retardance, and optic axis orientation [35,36]. Using the polarization information of myelin sheath, nerve fiber tracts as small as

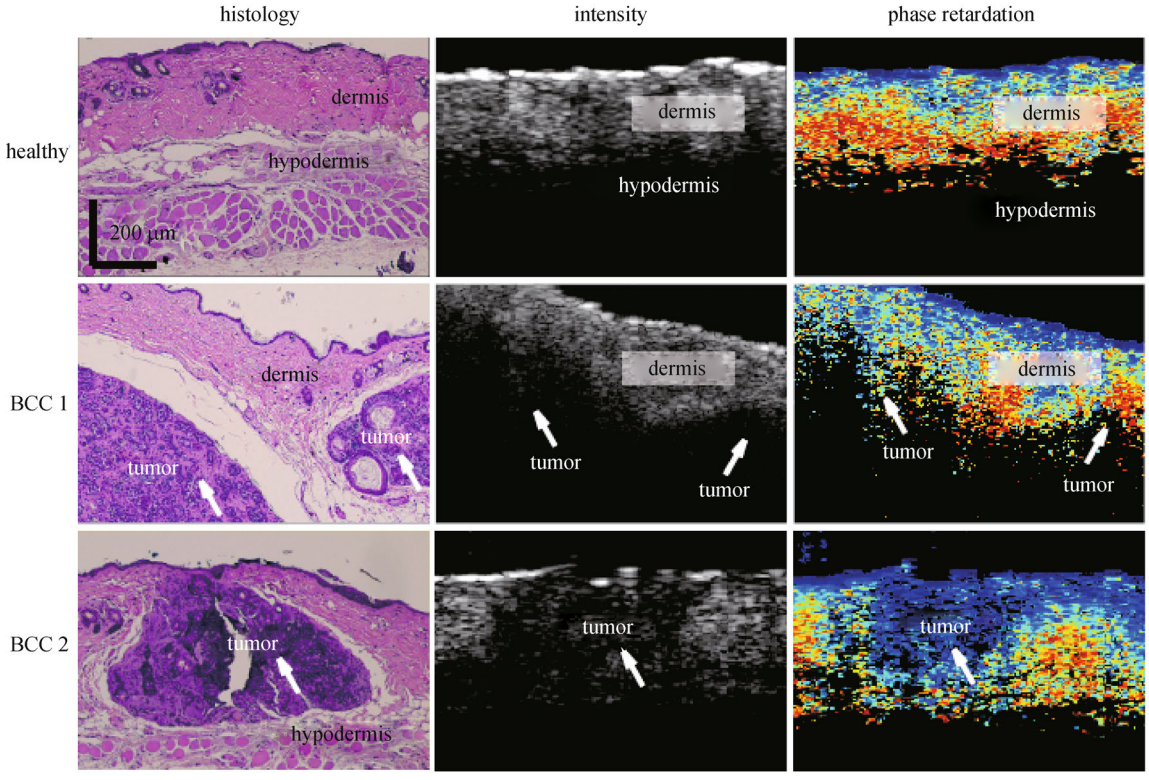

Fig. 6 Representative histological (left column), intensity (middle column), and phase retardation (right column) images obtained from the same or similar locations in healthy (top row), endogenous BCC (top row), and allograft BCC (bottom row) mouse skin tissue. White arrows indicate location of tumors. The scale bars are applicable to all images [11]. Reproduced from Ref. [11] with permission

a few tens of micrometers can be resolved and neighboring fiber tracts with different orientations can be distinguished in cross-sectional optical slices and 2D *en face* images. Figure 7 shows *en face* images reconstructed from the MC-OCT cross-sectional images to produce the sagittal view of the rat brain. Figures 7(a) and 7(b) are microscopy image and reflectivity of OCT, respectively. Figure 7(c) is the phase retardance map. Multiple fiber tracts in the midbrain are visible. Figure 7(d) is the optic axis orientation map. The arrows indicate three groups of fiber tracts with different orientations around the zona incerta. The use of axis orientation information enhances the identification of intermingled fiber tracts running across the viewing plane. Figure 7(e) shows the implementation of 2D tractography by utilizing phase retardance and optics axis orientation maps. The optics axis orientation and the retardance of fibers are encoded by color and brightness of the colors, respectively. MC-OCT images enable visualization of the spatial architecture and nerve fiber orientations in the brain with unprecedented detail. The results suggest that MC-OCT, by virtue of its direct accessibility to nerve fibers, has the potential to investigate structural connections in normal brain and neurological disorders [35]. In this system, the local phase retardance is calculated by differential retardance [35], which is valid only when the optics axis is not changed with the sample depth [50]. In addition, the optics axis orientation obtained by this system is also a cumulative value rather than local axis orientation information. To obtain local polarization information, more complex algorithms and system of two input polarization states [30,50,51] need to be considered. Therefore, selection of PS-OCT configuration for each application is a trade-off between the extracted information and system cost/complexity.

4 Conclusions

PS-OCT enables depth-resolved mapping of sample polarization information (such as phase-retardation and optical axis orientation), which is particularly useful when the nano-scale organization of tissue that are difficult to be observed in the intensity images of a regular OCT. This review summarizes several main methods and systems of PS-OCT, as well as its representative applications in biomedicine such as eye, skin, and brain. With further technology development, PS-OCT will become more reliable and easier to implement, therefore enabling more clinical applications in the near future.

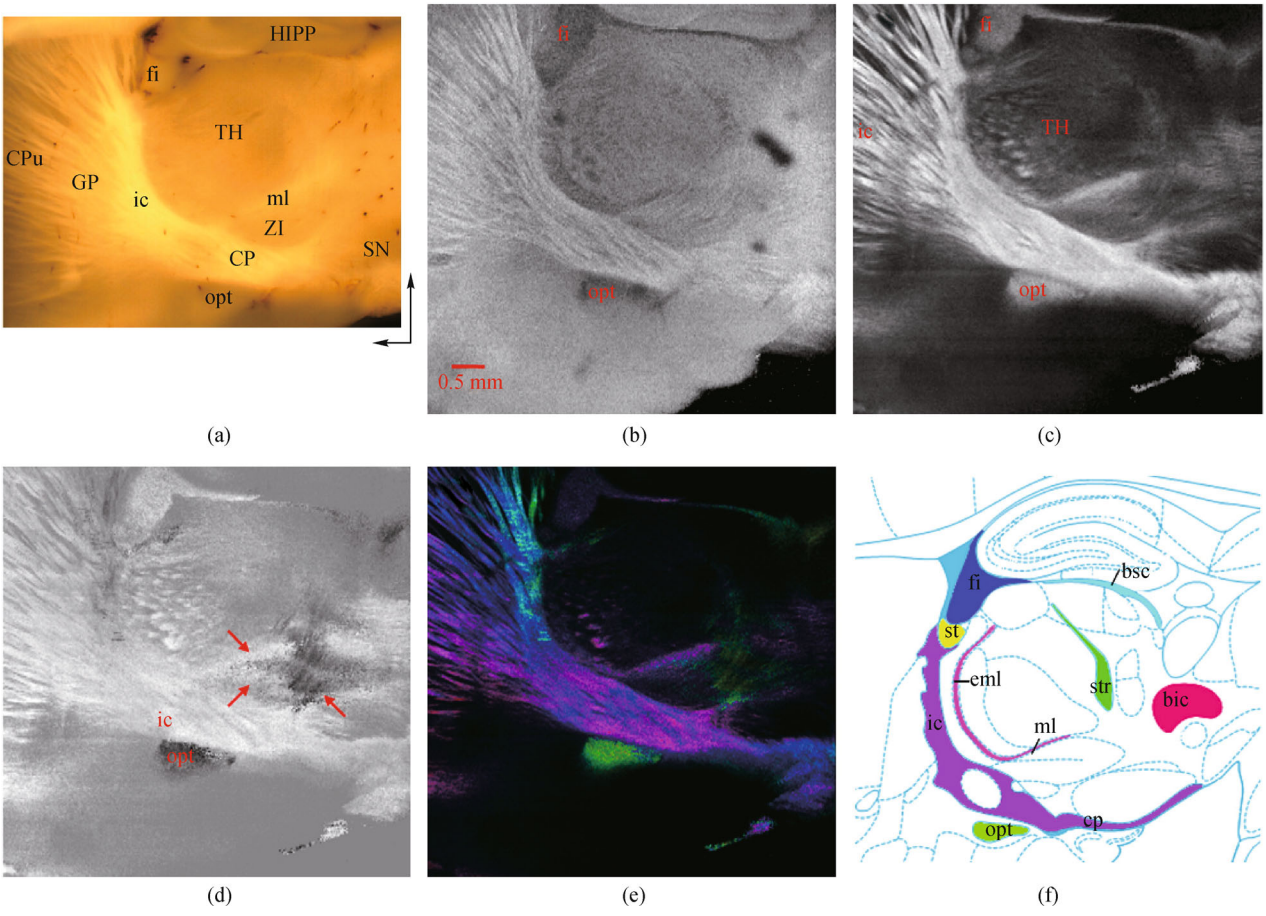

Fig. 7 Microscopy image (a) and reconstructed MC-OCT *en-face* images (b–d) of a sagittal rat brain section, with comparison of anatomy (f) [35]. Structures are labeled on the microscope image (a): cp, cerebral peduncle; CPu, caudate putamen; fi, fimbria; GP, globus pallidus; HIPP, hippocampus; ic, internal capsule; ml, medial lemniscus; opt, optic tract; SN, substania nigra; TH, thalamus; ZI, zona incerta. Leftward arrow: cranial; upward arrow: dorsal. Reconstructed brain maps of reflectivity (b), phase retardance (c), optic axis orientation (d) and combined image for tractography (e) are shown. The arrows in (d) indicate three groups of fiber bundles with different orientations. The image in (f) is modified from The Rat Brain in Stereotaxic Coordinates with permission. Abbreviations of structures: bic, brachium of the inferior colliculus; bsc, brachium of the superior colliculus; cp, cerebral peduncle; eml- external medullary lamina; fi-fimbria; ic, internal capsule; ml, medial lemniscus; opt, optic tract; st, stria terminalis; str, superior thalamic radiation [35]. Reproduced from Ref. [35] with permission

Acknowledgements This work was supported by the National Institutes of Health (NIH) (Grant Nos. R01DK094877, R21AG042700, R21DK088066 and R21EB012215), and the National Science Foundation (NSF) (Grant No. CBET-1254743) (CAREER Award). We acknowledge Qinggong Tang for helpful comments.

References

1. Hee M R, Huang D, Swanson E A, Fujimoto J G. Polarization-sensitive low-coherence reflectometer for birefringence characterization and ranging. Journal of the Optical Society of America. B, Optical Physics, 1992, 9(6): 903–908
2. Huang D, Swanson E A, Lin C P, Schuman J S, Stinson W G, Chang W, Hee M R, Flotte T, Gregory K, Puliafito C A. Optical coherence tomography. Science, 1991, 254(5035): 1178–1181
3. de Boer J, Srinivas S, Malekafzali A, Chen Z, Nelson J. Imaging thermally damaged tissue by polarization sensitive optical coherence tomography. Optics Express, 1998, 3(6): 212–218
4. Schoenenberger K, Colston B W, Maitland D J, Da Silva L B, Everett M J. Mapping of birefringence and thermal damage in tissue by use of polarization-sensitive optical coherence tomography. Applied Optics, 1998, 37(25): 6026–6036
5. Park B H, Saxer C, Srinivas S M, Nelson J S, de Boer J F. In vivo burn depth determination by high-speed fiber-based polarization sensitive optical coherence tomography. Journal of Biomedical Optics, 2001, 6(4): 474–479
6. Jiao S, Wang L V. Jones-matrix imaging of biological tissues with quadruple-channel optical coherence tomography. Journal of Biomedical Optics, 2002, 7(3): 350–358
7. Jiao S, Yu W, Stoica G, Wang L V. Contrast mechanisms in

polarization-sensitive Mueller-matrix optical coherence tomography and application in burn imaging. Applied Optics, 2003, 42(25): 5191–5197

8. Pierce M C, Strasswimmer J, Park B H, Cense B, de Boer J F. Advances in optical coherence tomography imaging for dermatology. The Journal of Investigative Dermatology, 2004, 123(3): 458–463
9. Srinivas S M, de Boer J F, Park H, Keikhanzadeh K, Huang H E, Zhang J, Jung W Q, Chen Z, Nelson J S. Determination of burn depth by polarization-sensitive optical coherence tomography. Journal of Biomedical Optics, 2004, 9(1): 207–212
10. Strasswimmer J, Pierce M C, Park B H, Neel V, de Boer J F. Polarization-sensitive optical coherence tomography of invasive basal cell carcinoma. Journal of Biomedical Optics, 2004, 9(2): 292–298
11. Duan L, Marvdashti T, Lee A, Tang J Y, Ellerbee A K. Automated identification of basal cell carcinoma by polarization-sensitive optical coherence tomography. Biomedical Optics Express, 2014, 5 (10): 3717–3729
12. Pircher M, Goetzinger E, Leitgeb R, Hitzenberger C K. Transversal phase resolved polarization sensitive optical coherence tomography. Physics in Medicine and Biology, 2004, 49(7): 1257–1263
13. Götzinger E, Pircher M, Sticker M, Fercher A F, Hitzenberger C K. Measurement and imaging of birefringent properties of the human cornea with phase-resolved, polarization-sensitive optical coherence tomography. Journal of Biomedical Optics, 2004, 9(1): 94–102
14. Ducros M G, de Boer J F, Huang H E, Chao L C, Chen Z P, Nelson J S, Milner T E, Rylander H III. Polarization sensitive optical coherence tomography of the rabbit eye. IEEE Journal on Selected Topics in Quantum Electronics, 1999, 5(4): 1159–1167
15. Ducros M G, Marsack J D, Rylander H G 3rd, Thomsen S L, Milner T E. Primate retina imaging with polarization-sensitive optical coherence tomography. Journal of the Optical Society of America A, Optics, Image Science, and Vision, 2001, 18(12): 2945–2956
16. Cense B, Chen T C, Park B H, Pierce M C, de Boer J F. *In vivo* birefringence and thickness measurements of the human retinal nerve fiber layer using polarization-sensitive optical coherence tomography. Journal of Biomedical Optics, 2004, 9(1): 121–125
17. Götzinger E, Pircher M, Hitzenberger C K. High speed spectral domain polarization sensitive optical coherence tomography of the human retina. Optics Express, 2005, 13(25): 10217–10229
18. Kemp N J, Park J, Zaatari H N, Rylander H G, Milner T E. High-sensitivity determination of birefringence in turbid media with enhanced polarization-sensitive optical coherence tomography. Journal of the Optical Society of America A, Optics, Image Science, and Vision, 2005, 22(3): 552–560
19. Baumann B, Choi W, Potsaid B, Huang D, Duker J S, Fujimoto J G. Swept source/Fourier domain polarization sensitive optical coherence tomography with a passive polarization delay unit. Optics Express, 2012, 20(9): 10229–10241
20. Götzinger E, Pircher M, Geitzenauer W, Ahlers C, Baumann B, Michels S, Schmidt-Erfurth U, Hitzenberger C K. Retinal pigment epithelium segmentation by polarization sensitive optical coherence tomography. Optics Express, 2008, 16(21): 16410–16422
21. Zotter S, Pircher M, Torzicky T, Baumann B, Yoshida H, Hirose F, Roberts P, Ritter M, Schütze C, Götzinger E, Trasischker W, Vass C, Schmidt-Erfurth U, Hitzenberger C K. Large-field high-speed polarization sensitive spectral domain OCT and its applications in ophthalmology. Biomedical Optics Express, 2012, 3(11): 2720–2732
22. Cense B, Chen T C, Park B H, Pierce M C, de Boer J F. Thickness and birefringence of healthy retinal nerve fiber layer tissue measured with polarization-sensitive optical coherence tomography. Investigative Ophthalmology & Visual Science, 2004, 45(8): 2606–2612
23. Makita S, Yamanari M, Yasuno Y. Generalized Jones matrix optical coherence tomography: performance and local birefringence imaging. Optics Express, 2010, 18(2): 854–876
24. Wang X J, Milner T E, de Boer J F, Zhang Y, Pashley D H, Nelson J S. Characterization of dentin and enamel by use of optical coherence tomography. Applied Optics, 1999, 38(10): 2092–2096
25. Baumgartner A, Dichtl S, Hitzenberger C K, Sattmann H, Robl B, Moritz A, Fercher A F, Sperr W. Polarization-sensitive optical coherence tomography of dental structures. Caries Research, 2000, 34(1): 59–69
26. Fried D, Xie J, Shafi S, Featherstone J D, Breunig T M, Le C. Imaging caries lesions and lesion progression with polarization sensitive optical coherence tomography. Journal of Biomedical Optics, 2002, 7(4): 618–627
27. Chen Y, Otis L, Piao D, Zhu Q. Characterization of dentin, enamel, and carious lesions by a polarization-sensitive optical coherence tomography system. Applied Optics, 2005, 44(11): 2041–2048
28. Jones R S, Darling C L, Featherstone J D, Fried D. Remineralization of *in vitro* dental caries assessed with polarization-sensitive optical coherence tomography. Journal of biomedical optics, 2006, 11(1): 014016
29. Pierce M, Shishkov M, Park B, Nassif N, Bouma B, Tearney G, de Boer J. Effects of sample arm motion in endoscopic polarization-sensitive optical coherence tomography. Optics Express, 2005, 13 (15): 5739–5749
30. Fan C, Yao G. Imaging myocardial fiber orientation using polarization sensitive optical coherence tomography. Biomedical Optics Express, 2013, 4(3): 460–465
31. Wang Y, Yao G. Optical tractography of the mouse heart using polarization-sensitive optical coherence tomography. Biomedical Optics Express, 2013, 4(11): 2540–2545
32. Hariri L P, Villiger M, Applegate M B, Mino-Kenudson M, Mark E J, Bouma B E, Suter M J. Seeing beyond the bronchoscope to increase the diagnostic yield of bronchoscopic biopsy. American Journal of Respiratory and Critical Care Medicine, 2013, 187(2): 125–129
33. Pasquesi J J, Schlachter S C, Boppart M D, Chaney E, Kaufman S J, Boppart S A. In vivo detection of exercised-induced ultrastructural changes in genetically-altered murine skeletal muscle using polarization-sensitive optical coherence tomography. Optics Express, 2006, 14(4): 1547–1556
34. Matcher S J, Winlove C P, Gangnus S V. The collagen structure of bovine intervertebral disc studied using polarization-sensitive optical coherence tomography. Physics in Medicine and Biology, 2004, 49(7): 1295–1306
35. Wang H, Black A J, Zhu J, Stigen T W, Al-Qaisi M K, Netoff T I,

Abosch A, Akkin T. Reconstructing micrometer-scale fiber pathways in the brain: multi-contrast optical coherence tomography based tractography. NeuroImage, 2011, 58(4): 984–992
36. Wang H, Zhu J, Akkin T. Serial optical coherence scanner for large-scale brain imaging at microscopic resolution. NeuroImage, 2014, 84: 1007–1017
37. Nakaji H, Kouyama N, Muragaki Y, Kawakami Y, Iseki H. Localization of nerve fiber bundles by polarization-sensitive optical coherence tomography. Journal of Neuroscience Methods, 2008, 174(1): 82–90
38. Al-Qaisi M K, Akkin T. Swept-source polarization-sensitive optical coherence tomography based on polarization-maintaining fiber. Optics Express, 2010, 18(4): 3392–3403
39. Hitzenberger C, Goetzinger E, Sticker M, Pircher M, Fercher A. Measurement and imaging of birefringence and optic axis orientation by phase resolved polarization sensitive optical coherence tomography. Optics Express, 2001, 9(13): 780–790
40. Wang H, Al-Qaisi M K, Akkin T. Polarization-maintaining fiber based polarization-sensitive optical coherence tomography in spectral domain. Optics Letters, 2010, 35(2): 154–156
41. de Boer J F, Milner T E. Review of polarization sensitive optical coherence tomography and Stokes vector determination. Journal of Biomedical Optics, 2002, 7(3): 359–371
42. Bonesi M, Sattmann H, Torzicky T, Zotter S, Baumann B, Pircher M, Götzinger E, Eigenwillig C, Wieser W, Huber R, Hitzenberger C K. High-speed polarization sensitive optical coherence tomography scan engine based on Fourier domain mode locked laser. Biomedical Optics Express, 2012, 3(11): 2987–3000
43. Trasischker W, Zotter S, Torzicky T, Baumann B, Haindl R, Pircher M, Hitzenberger C K. Single input state polarization sensitive swept source optical coherence tomography based on an all single mode fiber interferometer. Biomedical Optics Express, 2014, 5(8): 2798–2809
44. Ding Z, Liang C, Tang Q, Chen Y. Quantitative measurement of tissue birefringence by single mode fiber based PS-OCT with a single input polarization state using Muller matrix. Submitted to Biomedical Optics Express
45. Park B H, Pierce M C, Cense B, de Boer J F. Jones matrix analysis for a polarization-sensitive optical coherence tomography system using fiber-optic components. Optics Letters, 2004, 29(21): 2512–2514
46. Oh W Y, Yun S H, Vakoc B J, Shishkov M, Desjardins A E, Park B H, de Boer J F, Tearney G J, Bouma B E. High-speed polarization sensitive optical frequency domain imaging with frequency multiplexing. Optics Express, 2008, 16(2): 1096–1103
47. Fan C, Yao G. Mapping local retardance in birefringent samples using polarization sensitive optical coherence tomography. Optics Letters, 2012, 37(9): 1415–1417
48. Fan C, Yao G. Mapping local optical axis in birefringent samples using polarization-sensitive optical coherence tomography. Journal of Biomedical Optics, 2012, 17(11): 110501
49. Fan C, Yao G. Full-range spectral domain Jones matrix optical coherence tomography using a single spectral camera. Optics Express, 2012, 20(20): 22360–22371
50. Fan C, Yao G. Single camera spectral domain polarization-sensitive optical coherence tomography using offset B-scan modulation. Optics Express, 2010, 18(7): 7281–7287
51. Yamanari M, Makita S, Yasuno Y. Polarization-sensitive swept-source optical coherence tomography with continuous source polarization modulation. Optics Express, 2008, 16(8): 5892–5906
52. Guo S, Zhang J, Wang L, Nelson J S, Chen Z. Depth-resolved birefringence and differential optical axis orientation measurements with fiber-based polarization-sensitive optical coherence tomography. Optics Letters, 2004, 29(17): 2025–2027
53. Yun S, Tearney G, de Boer J, Bouma B. Removing the depth-degeneracy in optical frequency domain imaging with frequency shifting. Optics Express, 2004, 12(20): 4822–4828
54. Corsi F, Galtarossa A, Palmieri L. Polarization mode dispersion characterization of single-mode optical fiber using backscattering technique. Journal of Lightwave Technology, 1998, 16(10): 1832–1843
55. Park B, Pierce M, Cense B, de Boer J. Real-time multi-functional optical coherence tomography. Optics Express, 2003, 11(7): 782–793

Zhenyang Ding received the B.Sc., M.Sc., and Ph.D. degrees in optics engineering from Tianjin University, Tianjin, China, in 2008, 2010 and 2013, respectively. He is currently a postdoctoral research associate in Fischell Department of Bioengineering, University of Maryland, College Park, Maryland, USA. His current research interests include polarization-sensitive optical coherence tomography (PS-OCT) and representative biomedical applications. He has won Wang Daheng Optics Award for College Students, China, New academic Award by Ministry of Education, China, Excellent Doctorial Thesis Funding by Tianjin University, China, Graduate Student National Scholarship of China. Dr. Ding is a member of the Optical Society of America.

Chia-Pin Liang, who is currently a post-doctoral research fellow in Massachusetts General Hospital/Harvard Medical School, was a post-graduate course student of the National Cancer Institute-University of Maryland (NCI-UMD) joint program. Dr. Liang was awarded Ph.D. (bioengineering) degree from the University of Maryland, College Park. His interest is in developing novel biomedical imaging tools for clinicaluse and basic research.

Yu Chen is an Associate Professor of Bioengineering at the University of Maryland, College Park, USA. Dr. Chen received the B.S. degree in physics from Peking University in 1997, and the Ph.D. degree in bioengineering from University of Pennsylvania in 2003. His research interests encompass the areas of biomedical photonics and imaging, including optical coher-

ence tomography (OCT), multiphoton microscopy (MPM), needle-based endoscopy, and biomedical applications such as kidney imaging, brain mapping, and cancer detection. He has led numerous research projects funded by National Institutes of Health (NIH) and National Science Foundation (NSF), USA. He has published more than 60 peer-reviewed papers. Dr. Chen is a Fellow of the American Society for Laser Medicine and Surgery.